Rigorous Assessment of Natural Frequencies of Fault-Originated Travelling Waves

Zhaoyang Wang, *Member, IEEE,* Hamidreza Karami, *Member, IEEE,* Mario Paolone, *Fellow, IEEE,* and Pier Luigi Dragotti, *Fellow, IEEE*

***Abstract*—This paper presents a rigorous assessment of natural frequencies associated with fault-originated travelling waves in power networks, factoring in the presence of multiple junctions and branches. The proposed assessment exploits the Baum-Liu-Tesche (BLT) equation. An enhanced fault location accuracy is consequently attained leveraging rectified natural frequencies.**

***Index Terms*—Baum-Liu-Tesche equation, fault location, fault transients, natural frequencies, travelling waves**

I. Introduction

THE frequency-domain spectrum of fault-originated travelling waves (TWs) features the presence of distinct frequencies identified as natural or path-characteristic frequencies f_ps, which reflect the nature of the TWs propagating through different paths pertaining to a faulty power network [1]–[3]. In light of this, f_ps are employed in a dual capacity: firstly, as an indicator or metric for a fault event, functioning in the determination of its type and location (e.g., [1], [2]); secondly, the spectral attributes exhibited by the post-fault TWs at f_ps are leveraged as a foundational element by various other TW-based fault location (FL) methods (e.g., [3]).

Historically, there stands an analytical formula, demonstrating an inverse relationship (governed by a constant coefficient n_{p_i}) between a specific natural frequency f_{p_i} and the length L_{p_i} of its corresponding path p_i [1],

$$f_{p_i}^{\text{Ana}} = v/(n_{p_i} L_{p_i}), \tag{1}$$

where v is the TWs' propagation velocity. 'Ana' signifies the use of (1) to produce the estimate. However, it is imperative to clarify that (1) is established upon certain *assumptions*:

1. v remains constant and independent of frequency.

2. The boundary conditions are simplified to open circuits at an observation point (OP) and to short circuits at the fault location. Consequently, the coefficient n_{p_1} is determined to be 4 for the fault-related path (see p_1 in Fig. 1).

3. The discontinuities along a path caused by junctions are neglected. L_{p_i} is the length of the transmission line (TL) connecting an opted OP to a specific junction, terminal, or FL.

As a result, $f_{p_i}^{\text{Ana}}$ might be subjected to errors, especially in the context of complex power networks (e.g., a higher number of junctions). These errors afterwards lead to inaccuracies in FL when referencing the *a priori* f_ps. Also, note that the applicability of (1) is limited to homogeneous power networks.

This paper proposes that improved accuracy in estimating f_ps necessitates a detailed analysis of fault transients, which aims to adequately illustrate post-fault TW signals in the frequency domain by taking account of

- Topological (and existing inhomogeneous) features of targeted faulty power networks

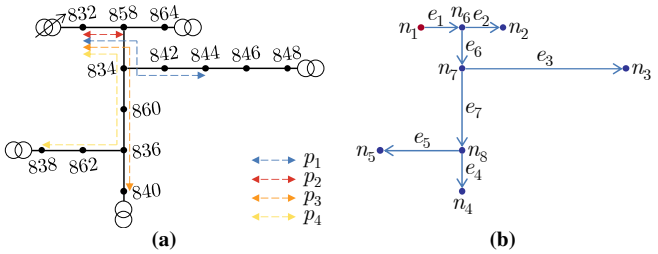

Fig. 1: IEEE 34-bus distribution feeder (the section with AC feeding at Bus 832). In the single-line diagram (a), a portion of the TW paths is depicted, wherein the fault-related path p_1 extends from the chosen OP Bus 832 to the FL Bus 844, passing through Buses 834 and 858. The directed-graph schematic (b) designates a terminal/junction as a *node* and a TL an *edge*. The direction of edge k dictates the positive direction of the coordinate x_k-axis and that of the current $I_k(x_k)$.

- Distributed and frequency-dependent attributes of TLs
- Scattering characteristics of connected power equipment
- Fault impedance (if it exists)

It is evident that the inclusion of the first two items allows for addressing the oversimplifications introduced by *assumptions 1* and *3*, while the remaining two items are directed towards *assumption 2*. The rigorous assessment of f_ps follows numerically solving fault transients in the frequency domain. The numerical analysis exploits the Baum-Liu-Tesche (BLT) equation (e.g., [4]) and specially adapts it to the FL problem.

II. Derivation of Modified BLT Equation

The ensuing derivation revolves round two-conductor TLs (2TLs)[1]. Let us refer back to the general solution for the voltage at the two terminals of a 2TL (e.g., Fig. 2):

$$\begin{cases} V_{(0)} = V^{+} + V^{-} = V^{re}(0) + V^{in}(0) \\ V_{(L)} = V^{+}e^{-\gamma L} + V^{-}e^{+\gamma L} = V^{in}(L) + V^{re}(L) \end{cases}, \tag{2}$$

where $V^{\pm}$ are undetermined constants dependent on frequencies. The superscripts '*re*' and '*in*' indicate the reflected and incident components, respectively. Also, note that to maintain brevity, evident frequency dependencies, like the one of the propagation constant γ, are not emphasized.

Given the scenario of Fig. 2a, where a 2TL is subjected to lumped excitation imposed by a series voltage source, Baum et al. derived the BLT equation as a compact matrix formula, by which the voltage responses at the terminals read:

$$\left[V_{(0)}\ V_{(L)}\right]^{\mathrm{T}} = \left(\boldsymbol{S} + \mathbf{1}_2\right)\left(\boldsymbol{S} - \boldsymbol{P}\right)^{-1}\boldsymbol{E}, \tag{3}$$

with $\boldsymbol{S}$, $\boldsymbol{P}$, and $\boldsymbol{E}$ being the frequency-dependent scattering matrix, propagation matrix, and excitation vector, respectively [4]. $\mathbf{1}_2$ represents the identity matrix of order 2.

[1]This focus is with the justifications: *i*) the derivation approach and results can be extended to multi-conductor TLs (MTLs) by using matrix notation; *ii*) 2TLs directly relate to existing power network configuration like mono-polar HVDC links; *iii*) each decoupled mode of MTLs is modelled in a 2TL circuit.

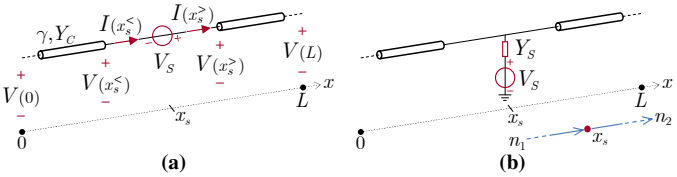

Fig. 2: A 2TL subjected to lumped excitation with (a) a series voltage source and (b) a shunt voltage source positioned at an arbitrary location along the line. (b) is accompanied by its directed graph.

On the other hand, considering the FL problem, fault-originated transients are typically simulated as the responses of a step function injected through a fault admittance (or impedance), as illustrated using V_S and Y_S in Fig. 2b. To likewise solve the terminal voltages, a re-derivation is necessary to specify $V^{\pm}$ in (2) following the provided boundary conditions.

With respect to the positive direction of the x-axis, $V^{+}e^{-\gamma x}$ and $V^{-}e^{+\gamma x}$ constitute the forward and backward TWs, respectively. Each is further recognized as either an incident or a reflected wave at the line terminals, as explained in (2). The incident and reflected waves can be related using the reflection coefficient S^{11}, which factors in the modelling and input impedance of terminal power equipment. As per the labelling of the two terminals as nodes 1 and 2 (see Fig. 2b), their re-spective S^{11} parameters are denoted S_1 and S_2.

At the assumed fault location, $x = x_s$, both the voltage and current are continuous prior to a fault event. That is

$$\boldsymbol{C}_{V,x_s}\boldsymbol{V}_{n,x_s} = \mathbf{1}_{2\times 1}, \text{and } \boldsymbol{C}_{I,x_s}\boldsymbol{I}_{n,x_s} = \mathbf{0}_{2\times 1}, \tag{4}$$

where, according to Fig. 2b,

$$\boldsymbol{V}_{n,x_s} = \left[V(x_s^<)\ V(x_s^>)\right]^{\mathrm{T}} \text{ and } \boldsymbol{I}_{n,x_s} = \left[-I(x_s^<)\ I(x_s^>)\right]^{\mathrm{T}}, \tag{5}$$

with the voltage and current connection matrices being

$$\boldsymbol{C}_{V,x_s} = \begin{bmatrix}1 & -1\end{bmatrix} \text{ and } \boldsymbol{C}_{I,x_s} = \begin{bmatrix}1 & 1\end{bmatrix}. \tag{6}$$

In the wake of injecting V_S (through Y_S), $x = x_s$ behaves as a plus-one junction, and thus the boundary condition holds

$$V(x_s^<) = V(x_s^>) = V_S + \left(I(x_s^<) - I(x_s^>)\right)/Y_S. \tag{7}$$

The combination of (4) and (7) yields

$$\left[V^{re}(x_s^<)\ V^{re}(x_s^>)\right]^{\mathrm{T}} = \boldsymbol{S}_{x_s}\left[V^{in}(x_s^<)\ V^{in}(x_s^>)\right]^{\mathrm{T}} + \boldsymbol{E}_{x_s}, \tag{8}$$

where $\boldsymbol{S}_{x_s}$ governs the interaction between the incident waves and the reflected ones. It is a 2×2 matrix solved by

$$\boldsymbol{S}_{x_s} = \begin{bmatrix} -\boldsymbol{C}_{V,x_s} \\ \hdashline \boldsymbol{C}_{I,x_s}(\boldsymbol{Y}_{C,x_s} + \boldsymbol{Y}_S) \end{bmatrix}^{-1} \begin{bmatrix} \boldsymbol{C}_{V,x_s} \\ \hdashline \boldsymbol{C}_{I,x_s}(\boldsymbol{Y}_{C,x_s} - \boldsymbol{Y}_S) \end{bmatrix} \tag{9}$$

with

$$\boldsymbol{Y}_{C,x_s} = \mathrm{diag}\left(Y_C, Y_C\right) \text{ and } \boldsymbol{Y}_S = \mathrm{diag}\left(Y_S, 0\right). \tag{10}$$

Moreover, the added excitation vector $\boldsymbol{E}_{x_s}$, which illustrates the fault effect (i.e., the voltage injection), is derived as

$$\boldsymbol{E}_{x_s} = \begin{bmatrix} -\boldsymbol{C}_{V,x_s} \\ \hdashline \boldsymbol{C}_{I,x_s}(\boldsymbol{Y}_{C,x_s} + \boldsymbol{Y}_S) \end{bmatrix}^{-1} \begin{bmatrix} \\ \hdashline Y_S V_S \end{bmatrix} \tag{11}$$

Through the integration of the four sets of incident and reflected waves, the first matrix equation can be formulated, encompassing the scattering matrix and the excitation vector:

$$\begin{bmatrix} V^{re}(0) \\ \hdashline V^{re}(x_s^<) \\ V^{re}(x_s^>) \\ \hdashline V^{re}(L) \end{bmatrix} = \begin{bmatrix} S_1 & & \\ & \boldsymbol{S}_{x_s} & \\ & & S_2 \end{bmatrix} \begin{bmatrix} V^{in}(0) \\ \hdashline V^{in}(x_s^<) \\ V^{in}(x_s^>) \\ \hdashline V^{in}(L) \end{bmatrix} + \begin{bmatrix} \\ \hdashline \boldsymbol{E}_{x_s} \\ \hdashline \end{bmatrix}. \tag{12}$$

Let $\boldsymbol{V}_n^{in}$ and $\boldsymbol{V}_n^{re}$ refer to the vector of incident and reflected waves. Then, (12) can be rewritten as

$$\boldsymbol{V}_n^{re} = \boldsymbol{S}\boldsymbol{V}_n^{in} + \boldsymbol{E}, \tag{13}$$

where, following (3), the scattering supermatrix is denoted as $\boldsymbol{S}$ (the same applies to $\boldsymbol{P}$ and $\boldsymbol{E}$ hereinafter).

In light of $x = x_s$ being an additional junction, the propagation supermatrix is derived from (2) as

$$\boldsymbol{P} = \mathrm{diag}\left(\begin{bmatrix} & e^{+\gamma x_s} \\ e^{+\gamma x_s} & \end{bmatrix}, \begin{bmatrix} & e^{+\gamma(L-x_s)} \\ e^{+\gamma(L-x_s)} & \end{bmatrix}\right), \tag{14}$$

which allows the second matrix equation to be established:

$$\boldsymbol{V}_n^{re} = \boldsymbol{P}\boldsymbol{V}_n^{in}. \tag{15}$$

Synthesizing (13) and (15) results in solving

$$\boldsymbol{V}_n^{in} = \left(\boldsymbol{P} - \boldsymbol{S}\right)^{-1}. \tag{16}$$

The addition of $\boldsymbol{V}_n^{in}$ and $\boldsymbol{V}_n^{re}$, using (15) and (16), yields

$$\boldsymbol{V}_n = \left(\boldsymbol{P} + \mathbf{1}_4\right)\left(\boldsymbol{P} - \boldsymbol{S}\right)^{-1}\boldsymbol{E}, \tag{17}$$

where

$$\boldsymbol{V}_n = \left[\, V(0) \,\middle\vdots\, V(x_s^<)\ \ V(x_s^>) \,\middle\vdots\, V(L) \,\right]^{\mathrm{T}}. \tag{18}$$

So far, (17) retrieves a compact matrix formula for solving the terminal responses in the FL problem. Observe its modification to the BLT equation (3), including the rearrangement of the first two terms and the involved matrix/vector terms being reconstructed (in terms of their dimension and elements).

III. Solution for Fault Transients in Complex Power Networks Using Modified BLT Equation

The modified BLT equation (17) is applicable in analysing fault transients in complex power networks that feature multiple junctions and branches, along with inhomogeneity. Without losing generality, this section illustrates the analysis approach using the power network depicted in Fig. 1 as a reference.

The directed graph Fig. 1b decomposes the power network into seven edges. A node voltage vector is constructed for each edge by combining the voltage at the associated two nodes

$$\boldsymbol{V}_{n,e_k} = \left[V_k(0)\ \ V_k(L_k)\right],\ k = 1, 2, \ldots, 7. \tag{19}$$

Note that when edge K ($K \in k$) is presumed to be the faulty branch, it is viewed as consisting of two sub-edges because of the addition of an FL along it, as explained by (7). In this case, $\boldsymbol{V}_{n,e_K}$ complies with (18). By stacking these node voltage vectors based on the edge numbers in ascending order, the resulting 16×1 overall node voltage supervector is

$$\boldsymbol{\mathcal{V}}_{n\ 16\times 1} = \left[\ \boldsymbol{V}_{n,e_1} \,\middle\vdots\, \ldots \,\middle\vdots\, \boldsymbol{V}_{n,e_7}\ \right]^{\mathrm{T}}. \tag{20}$$

In a similar fashion, the integrated propagation supermatrix with the dimension of 16 by 16 is structured as

$$\boldsymbol{\mathcal{P}}_{16\times 16} = \mathrm{diag}\left(\boldsymbol{P}_{e_1},\ \ldots,\ \boldsymbol{P}_{e_7}\right), \tag{21}$$

in which $\boldsymbol{P}_{e_K}$ is specified taking the form of (14), while the remaining sub-matrices can be derived according to (2) as

$$\boldsymbol{P}_{e_k} = \begin{bmatrix} & e^{+\gamma_k L_k} \\ e^{+\gamma_k L_k} & \end{bmatrix},\ k \in \complement_{\{1,2,\ldots,7\}}K. \tag{22}$$

To illustrate the formulation of the overall scattering matrix $\boldsymbol{\mathcal{S}}$, we assume a fault event along the TL of edge 3, with K specified as 3. Nodes 1 to 5 are the terminals of their respective branches. Each node is thus characterized by a single reflection coefficient S^{11}, labelled S_1 through S_5. For instance, take S_5, which is placed in the cell indexed $(12, 12)$ in $\boldsymbol{\mathcal{S}}$,

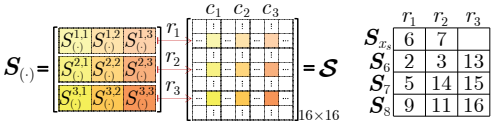

Fig. 3: Graphical illustration of mapping the scattering matrices $\boldsymbol{S}_6$ to $\boldsymbol{S}_8$ and $\boldsymbol{S}_{x_s}$ into the overall scattering matrix $\boldsymbol{\mathcal{S}}$. For each among $\boldsymbol{S}_6$ to $\boldsymbol{S}_8$, its three rows in ascending row order are mapped into the rows numbered r_1, r_2, and r_3 of $\boldsymbol{\mathcal{S}}$, respectively. The arrangement of columns mirrors this pattern, with the column numbers c_1, c_2, and c_3 being the same as r_1, r_2, and r_3, respectively. When applied to $\boldsymbol{S}_{x_s}$, the mapping process is adjusted to involve two rows and two columns. The accompanying table lists the values of r_1 to r_3, aligning with the assumption that edge 3 is the faulty branch.

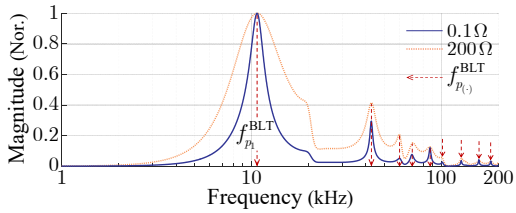

Fig. 4: Magnitude spectrum of $V_{1(0)}$ related to the 1p-g fault cases at Bus 846. The local peaks in magnitudes of $V_{1(0)}$ align closely in terms of f_ps for fault impedances of 0.1 Ω and 200 Ω, respectively.

corresponding to the assignment of $V_{5(L_5)}$ with index 12 in $\boldsymbol{\mathcal{V}}_n$ as per (20). Likewise, S_1 to S_4 are arranged along the diagonal of $\boldsymbol{\mathcal{S}}$ at rows 1, 4, 8, and 10, respectively. Nodes 6 to 8 each are junctions where three TLs come to an end. The scattering characteristics are thus governed by a 3×3 scattering matrix, namely $\boldsymbol{S}_6$ to $\boldsymbol{S}_8$. For example, the interaction among $V_{1(L_1)}$, $V_{2(0)}$, and $V_{3(0)}$ occurs at node 6. Consistent with the indexing of the three voltages as 2, 3, and 13 in $\boldsymbol{\mathcal{V}}_n$, the elements of $\boldsymbol{S}_6$ are distributed within $\boldsymbol{\mathcal{S}}$ at the intersections of rows and columns 2, 3, and 13 (see Fig. 3). The scattering matrix of the fault location, $\boldsymbol{S}_{x_s}$, is given in (9). Its positioning in $\boldsymbol{\mathcal{S}}$ refers to the indices of $V_{3(x_s^<)}$ and $V_{3(x_s^>)}$ in $\boldsymbol{\mathcal{V}}_n$.

Finally, the overall excitation supervector $\boldsymbol{\mathcal{E}}$ exhibits sparsity with solely the $K^{\text{-th}}$ sub-vector, $\boldsymbol{E}_{e_K}$, showcasing non-zero elements. $\boldsymbol{E}_{e_K}$ is identified by referencing (12) and (13). Specific to the illustrated case, $\boldsymbol{\mathcal{E}}$ is structured as

$$\boldsymbol{\mathcal{E}}_{16\times 1} = \left[\ \mathbf{0}_{1\times 2} \ \middle|\ \mathbf{0}_{1\times 2} \ \middle|\ \boldsymbol{E}_{e_3} \ \middle|\ \mathbf{0}_{1\times 2} \ \middle|\ \dots \ \right]^{\mathrm{T}}. \tag{23}$$

Substituting the matrix terms of (17) with the counterparts derived from the above system-wide analysis results in

$$\boldsymbol{\mathcal{V}}_n = (\boldsymbol{\mathcal{P}} + \mathbf{1}_{16})\,(\boldsymbol{\mathcal{P}} - \boldsymbol{\mathcal{S}})^{-1}\,\boldsymbol{\mathcal{E}}. \tag{24}$$

It covers the voltages observed at all terminals and junctions in response to a fault occurrence with its location and impedance being assumed. Refer to Fig. 4 for an example of the magnitude spectrum of $V_{1(0)}$, illustrating the post-fault TW voltage signal observed at Bus 832, for 1p-g fault cases at Bus 846[2].

IV. Conclusion

We conclude this paper by showcasing the enhanced estimation of f_ps, and thereby, the improved accuracy in FL achieved through the use of (24).

In the spectrum of the solved fault transient, the frequency point featuring the first dominant component is identified as

[2]For comparative analyses, the implementation of (24) matches the parameter settings of [1]: mode-0 parameters are utilized to analyse single-phase solid (1p-g) faults and mode-1 ones for three-phase solid (3p-g) faults. The sampling rate is 10 MHz. The fault impedance is set at 0.1 Ω (i.e., Y_S as 10 S). The input impedance of all terminal transformers is modelled as 10 kΩ.

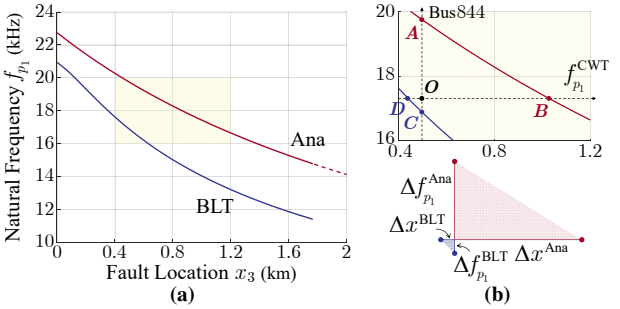

Fig. 5: (a) Estimated f_{p_1} as a function of the FL (defined at 1-meter intervals) along the TL of edge 3 for 3p-g faults. (b) The enlarged view of the colour-filled area in Fig. 5a. The horizontal line, marked at the ordinate $f_{p_1}^{\text{CWT}}$, intersects the vertical line at the abscissa of Bus 844 at point O. The horizontal line, along with the vertical one, intersect the two x_3-f_{p_1} curves at four distinct points labelled A to D. The five points form two right triangles. $\Delta f_{p_1}^{\text{Ana}}$ and $\Delta f_{p_1}^{\text{BLT}}$ are identifiable as the two vertical legs. Δx^{Ana} and Δx^{BLT} are recognised as the two horizontal legs.

the natural frequency of the fault-related path (i.e., p_1 in Fig. 1a), corresponding to $f_{p_1}^{\text{BLT}}$ identified within $|V_{1(0)}|$ of Fig. 4. Extending this analysis to a set of assumed FLs along the TL of edge 3, the resulting pairs of x_3-$f_{p_1}^{\text{BLT}}$ mapping relationship can be visually represented by the curve depicted in Fig. 5a. The curve x_3-$f_{p_1}^{\text{Ana}}$ is likewise obtained referring to (1). To assess the accuracy attained, these *a priori* estimates are compared with their post-fault counterparts according to $\Delta f_{p_1}^{(\cdot)}$ as $|f_{p_1}^{(\cdot)} - f_{p_1}^{\text{CWT}}|$, with '$(\cdot)$' being held for 'Ana' and 'BLT'. The values of $f_{p_1}^{\text{CWT}}$ are referenced in [1], as a result of utilizing the continuous wavelet transform (CWT) to identify f_{p_1} within post-fault TW signals. Table I presents the results of applying the analysis outlined above to all buses shown in Fig. 1a, covering both 1p-g and 3p-g faults. It is clear that, between $f_{p_1}^{\text{Ana}}$s and $f_{p_1}^{\text{BLT}}$s, $f_{p_1}^{\text{CWT}}$s converge more closely to the latter, with a single exception being the 3p-g fault case at Bus 864. In the other cases, the averaged value of $\Delta f_{p_1}^{\text{BLT}}$s is 0.61 kHz for the 1p-g fault cases and 0.42 kHz for the 3p-g ones, in contrast to $\Delta f_{p_1}^{\text{Ana}}$, which averages 1.44 kHz and 2.04 kHz, respectively. The most notable improvement is observed at Bus 848's 3p-g fault case, achieving 0.2 kHz against 3.16 kHz.

The refined estimation of f_ps is pivotal in facilitating their dual function in FL, leading to enhanced accuracy. The diagrammatic explanation in Fig. 5b indicates that the abscissae of the intersection points B and D match the FLs as estimated by tracing the respective curves of x_3-f_{p_1}. The corresponding FL errors, Δx^{Ana} and Δx^{BLT}, are quantified as the absolute differences between the estimated values and the true FL's abscissa. In Table II, the results listed in the 'Δx^{Ana}' columns, as cited from [1], include a noticeable portion of the errors exceeding 300 m, a level of accuracy achievable by GPS-aided TW methods [5]. Contrastingly, with one exception, the values of Δx^{BLT} are shown to be largely below 300 m. The 3p-g fault case at Bus 848 is notable for an optimal reduction in the error, from 1374.2 m to 75.8 m. Among the FL methods that rely on f_p-related spectral attributes, the time-reversal (TR) category is considered for examination. It is observed that the reversed-time fault current exhibits energy concentration at f_ps [3]. Specific to the fault cases analysed, for each predefined FL, (24) solves its corresponding fault transient $V_{1(0)}$ and subsequently pinpoints f_ps at those frequencies where $V_{1(0)}$ exhibits a local

TABLE I: Estimates of f_{p_1} and Their Absolute Differences Relative to the Referenced CWT Counterparts (Values in kHz)

FL (Bus)	Single-phase solid (1p-g) fault		Three-phase solid (3p-g) fault	
	$f_{p_1}^{\text{Ana}}(\Delta f_{p_1}^{\text{Ana}})$	$f_{p_1}^{\text{BLT}}(\Delta f_{p_1}^{\text{BLT}})$	$f_{p_1}^{\text{Ana}}(\Delta f_{p_1}^{\text{Ana}})$	$f_{p_1}^{\text{BLT}}(\Delta f_{p_1}^{\text{BLT}})$
834	20.59 (1.29)	18.94 (0.36)	22.75 (1.55)	20.95 (0.25)
836	14.29 (1.29)	12.28 (0.72)	15.80 (2.10)	13.58 (0.12)
838	10.72 (1.02)	8.93 (0.77)	11.85 (1.45)	9.90 (0.50)
840	13.55 (1.35)	11.52 (0.68)	15.08 (1.88)	12.74 (0.46)
842	20.04 (1.04)	18.41 (0.59)	22.14 (1.44)	20.33 (0.37)
844	17.86 (2.06)	15.30 (0.50)	19.87 (2.57)	16.90 (0.40)
846	13.80 (2.50)	10.69 (0.61)	15.35 (3.05)	11.84 (0.46)
848	13.36 (2.36)	10.29 (0.71)	14.76 (3.16)	11.40 (0.20)
858	45.18 (0.28)	45.09 (0.19)	49.94 (1.34)	49.83 (1.23)
860	17.31 (1.11)	15.50 (0.70)	19.26 (1.66)	17.13 (0.57)
862	14.03 (1.33)	12.03 (0.67)	15.61 (2.21)	13.30 (0.10)
864	34.00 (1.60)	34.81 (0.79)	37.84 (0.06)	38.42 (0.52)

TABLE II: Fault Location Errors Resulting from the Application of the Two Types of f_p-Based Methods (Values in Meters)

FL (Bus)	Single-phase solid (1p-g) fault			Three-phase solid (3p-g) fault		
	Δx^{Ana}	Δx^{BLT}	$\Delta x^{\text{BLT-TR}}$	Δx^{Ana}	Δx^{BLT}	$\Delta x^{\text{BLT-TR}}$
834	218.2	60.0	1.0	239.7	38.0	1.0
836	468.7	219.6	0.6	721.0	34.6	0.6
838	660.5	468.7	0.7	874.3	292.7	6.8
840	548.2	235.1	0.1	706.1	146.1	0.1
842	183.3	84.3	19.4	234.4	50.3	5.5
844	490.9	73.8	1.0	560.9	54.8	1.0
846	1077.7	214.3	0.1	1211.5	150.3	0.1
848	1080.2	274.8	0.9	1374.2	75.8	0.9
858	9.4	0.5	0.5	41.0	0.5	0.5
860	265.7	135.7	7.6	367.1	83.7	7.6
862	500.9	84.3	0.6	791.4	30.3	6.8
864	88.9	63.8	8.5	3.1	0.8	0.8

peak in magnitude. During the FL process, each predefined FL is assigned an energy value, which is calculated by aggregating the squared modulus of the fault current components present at the estimated f_ps linked to the FL. The location with the highest energy value is identified as the estimated FL. As evidenced by the results under the header $\Delta x^{\text{BLT-TR}}$, the energy metric further diminishes the FL errors to a minimal level.

The analyses above indicate that the two types of FL methods are implemented through a data-driven strategy, as exemplified in [6]. Specifically, the estimation of f_ps is conducted prior to actual fault events, utilizing the parameters of targeted power networks. This preparatory step yields a database that indexes the estimates of f_ps for a set of user-defined FLs. The online process examines post-fault TW signals with reference to the *a priori* f_ps across the database to identify the true FL. Also, given the closely aligned behaviour observed in Fig. 4, it is feasible to assume near-zero fault impedance for locating both solid faults and those with relatively small impedance.

REFERENCES

[1] A. Borghetti, M. Bosetti, M. D. Silvestro, C. A. Nucci, and M. Paolone, "Continuous-Wavelet Transform for Fault Location in Distribution Power Networks : Definition of Mother Wavelets Inferred From Fault Originated Transients," *IEEE Trans. Power Syst.*, vol. 23, no. 2, pp. 380–388, 2008.

[2] S. He, A. Cozza, and Y. Xie, "Fault-Location Accuracy of Natural Frequencies Using Incomplete HVDC Station Models," *IEEE Trans. Power Deliv.*, vol. 38, no. 5, pp. 3677–3687, 2023.

[3] H. Cui, Q. Yang, J. Sun, T. Zhou, and Y. He, "Electromagnetic Time Reversal Fault Location Method Based on Characteristic Frequency of Traveling Waves," *IEEE Trans. Power Deliv.*, vol. 38, no. 5, pp. 3033–3044, 2023.

[4] F. M. Tesche, M. Ianoz, and T. Karlsson, *EMC Analysis Methods and Computational Models*. Wiley, 1996.

[5] E. O. Schweitzer, A. Guzman, M. V. Mynam, V. Skendzic, B. Kasztenny, and S. Marx, "Locating Faults by the Traveling Waves They Launch," *2014 67th Annual Conference for Protective Relay Engineers, CPRE 2014*, pp. 95–110, 2014.

[6] Z. Wang, Z. Chen, and M. Paolone, "A Data-Driven Fault Location Algorithm Based on the Electromagnetic Time Reversal in Mismatched Media," *IEEE Trans. Power Deliv.*, vol. 37, no. 5, pp. 3709–3721, 2022.